Space Vector Modulation for High Dynamic Current Control of a Self-Sensing Active Magnetic Bearing

Dominik Wimmer, Markus Hutterer, and Manfred Schrödl

Institute of Energy Systems and Electrical Drives
Technische Universität Wien
Gußhausstraße 25, 1040 Vienna, Austria
`dominik.wimmer@tuwien.ac.at`

Abstract

The control loop of active magnetic bearings requires feedback of the rotor position to enable a stable levitation of the rotor. In contrast to conventional position sensor-based systems, self-sensing control can lead to a far more simple design of the system. The focus of this study lies on a high dynamic control of a self-sensing three-phase radial active magnetic bearing. The self-sensing operation is based on the detection of coil inductance deviations of an eccentrically levitating rotor. The inductance of the actuator coils is obtained by current slope measurements in the phases of the bearing. For this reason, special voltage pulse patterns are applied to the coils, which are defined by the half-bridges of a three-phase inverter. The required voltage pulse patterns are defined by a space vector modulation in a digital signal processor. In this work, a variant of space vector modulation is presented, which allows a high dynamic of the current controller under consideration of self-sensing aspects. Finally, the designed modulation strategy was investigated with simulations and measurements on a prototype of a radial active magnetic bearing.

1 Introduction

Active magnetic bearings (AMBs) enable a stable levitation of a rotor without mechanical contact. Therefore, high rotor speeds can be reached without the need of lubricants. For a stable levitation of the rotor, a position information of the rotor is required to close the control loop. Conventional AMB systems use position sensors to determine the rotor position. Design criteria of active magnetic bearings often include requirements like system costs, construction space and the reliability of the system. Self-sensing methods can help to achieve the design goals by a reduction of the number of sensors in a system. The self-sensing control of active magnetic bearings is a field of research for many years [1]. Therefore, various control approaches have been established, which can be divided in observer-based and high frequency perturbation methods [2]. Observer-based methods rely on a design of an estimator for the air gap length by voltage and current measurements. Therefore, a detailed mathematical description of the system is required to achieve adequate estimator results as shown in [3]. High frequency perturbation methods rely on an estimation of the air gap length by the inductance of the actor. In many AMB configurations, the air gap length influences the inductance of the actuator coils. Hence, inductance changes can be detected by the current response of high frequency (HF) voltage pulses. Previous studies in this field used switching amplifiers with hysteresis [4], [5], HF voltage injection [6], [7] or an analysis of the current ripple by the pulse width modulation (PWM) in time or frequency domain [8]–[13].

In this study, a modified version of the so-called INFORM (Indirect Flux detection by Online Reluctance Measurement) method is used for the detection of the rotor position. The method

was originally designed for the rotor angle estimation of permanent magnet synchronous motors [14]. In previous studies, the INFORM method was adapted to three-phase active magnetic bearings, enabling a self-sensing control of the rotor position [15], [16]. The method is based on current slope measurements to detect inductance deviations of an eccentrically levitating rotor. Therefore, special voltage pulse patterns are applied to the actuator coils by the switches of a three-phase inverter. The voltage pulse patterns are defined by a space vector modulation, which is an essential element of the proposed self-sensing control method. On the one hand, the space vector modulation has to provide the desired output voltage for the control of the coil currents. On the other hand, the space vector modulation must ensure the possibility of current slope measurements by the fulfillment of timing requirements of the pulse pattern.

The following article deals with the design of a space vector modulation, which enables a high bandwidth of the current controller as well as a suitability for self-sensing control. In previous work, control current deviations were observed by a switchover of the space vector modulation strategy, which may lead to limitations in high precision control [17]. For that reason, special attention is paid to a precise control of the coil currents. In the following, the self-sensing principle is briefly outlined and requirements as well as limitations of space vector modulation (SVM) are discussed. Considering the design rules, a novel variant of SVM is introduced and implemented in a digital signal processor (DSP). Measurements on a prototype show the achievable current controller performance compared to a previous SVM strategy.

2   Self-Sensing Principle

The self-sensing principle is briefly outlined to introduce the requirements of self-sensing space vector modulation. The bearing configuration of Fig. 1 shows a three-phase radial AMB with six poles. The bias flux of the homopolar design is realized by permanent magnets. For the use of a conventional three-phase inverter, the coils are connected in a double wye configuration. The
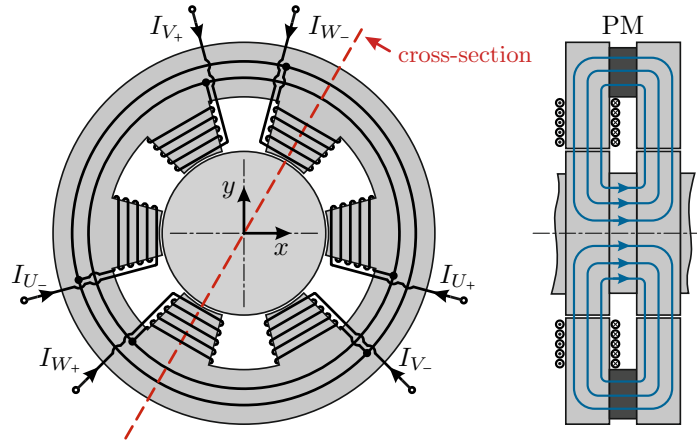

Figure 1: Structural design of the six pole radial homopolar AMB with a cross-section of the shaft. The bias flux (indicated by blue lines) is generated by permanent magnets (PM).

detection of the rotor position is based on the evaluation of the position dependent inductance of the actuator coils. Therefore, voltage pulses are applied to the coils, which are defined by the half bridges of a three-phase inverter. In simplification, the inductance can be determined

by a measurement of the current slope $\mathrm{d}I/\mathrm{d}t$ due to a defined voltage pulse.

$$U \approx L \cdot \frac{\mathrm{d}I}{\mathrm{d}t} \rightarrow L \approx U \cdot \left(\frac{\mathrm{d}I}{\mathrm{d}t}\right)^{-1} \tag{1}$$

Concerning the rotor position detection, the inductance variation of opposing coils plays an important role. For this reason, an approach with a differential evaluation of opposing coil currents was chosen to cancel out inductance offsets. The determination of the inductance variation is based on a differential current slope measurement of the actuator coils. In this configuration, the differential current slope is measured by a transformer with an open-circuited sense winding as shown in Fig. 2. The transformer builds the connection between two opposing
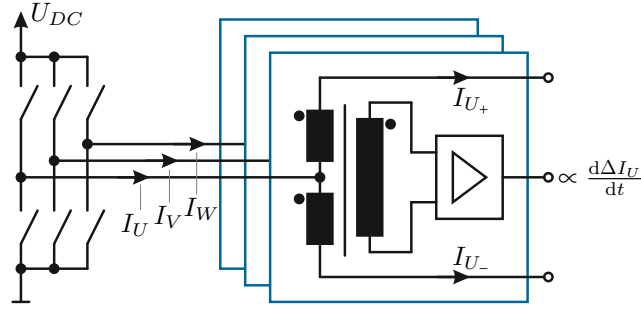

Figure 2: Illustration of the three-phase differential current slope measurement.

coils of the bearing and a phase of the inverter. Therefore, the differential design of the transformer enables the measurement of the differential current slope $\mathrm{d}\Delta I/\mathrm{d}t$ with $\Delta I = I_+ - I_-$ [18]. Thus, the rotor position can be calculated with the $\mathrm{d}\Delta I/\mathrm{d}t$ information under the consideration of the reluctance model of the three-phase magnetic circuit [16]. Concerning the settling time of the transformer, a minimal pulse width of the applied voltage pulses is required to allow a stable measurement of the current slope $\mathrm{d}\Delta I/\mathrm{d}t$. Figure 3 shows an exemplary waveform of the differential current ΔI_U and the output voltage of the transformer, which is proportional
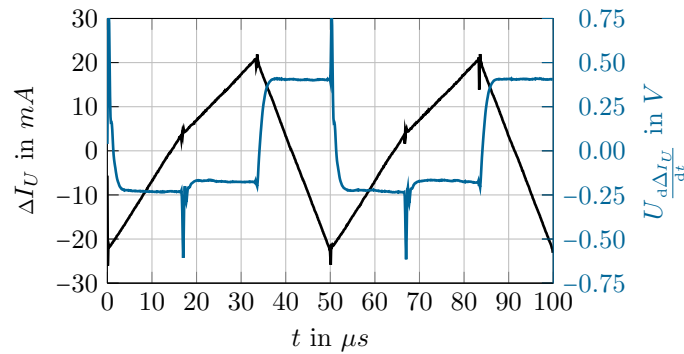

Figure 3: Current slope detection: The output voltage of the transformer $U_{\mathrm{d}\Delta I_U/\mathrm{d}t}$ is proportional to the differential current slope of the AMB phase U. ($f_{PWM} = 20\,kHz$)

to the derivative of the signal. It can be seen that the output voltage is nearly constant after the settling time of the transformer. Thus, it can be concluded that the presented procedure

requires a minimum voltage pulse width to enable a proper determination of the current slope information, which must be guaranteed by the space vector modulation.

3   Space Vector Modulation

The three-phase design of the AMB enables the usage of a space vector modulation, which is responsible for applying the respective control voltage to the AMB coils. Figure 4 shows an overview of the interaction between current controller, space vector modulation and the
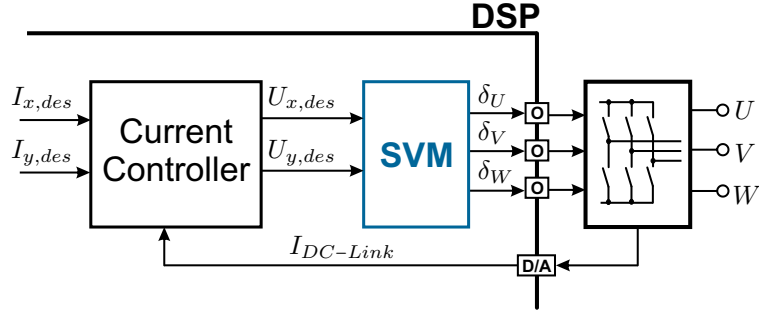

Figure 4: Structural overview of the current control loop: The SVM defines the duty cycles of the half-bridges correspondingly to the desired phase voltages of the current controller. The current feedback is realized by a measurement of the DC-Link current $I_{DC-Link}$.

half-bridges of the inverter. For achieving the force requirements of a superimposed position controller, the respective control currents ($I_{x,des}$, $I_{y,des}$) must be regulated in the AMB coils. Therefore, the current controller demands the desired coil voltages ($U_{x,des}$, $U_{y,des}$), which are the inputs of the SVM.

$$\boldsymbol{P} = \begin{bmatrix} U_{x,des} \\ U_{y,des} \end{bmatrix} \tag{2}$$

The SVM calculates the duty cycles δ_U, δ_V, δ_W correspondingly to the desired coil voltage space vector $\boldsymbol{P}$, whereby the timing of the switches of the three half-bridges is defined. The topology of the three-phase inverter enables the definition of eight fundamental voltage space vectors by the switches of the half-bridges as shown in Table 1. If the voltage transition during the

Table 1: Voltage space vector definition of a three-phase inverter

Phase	Switch	Voltage space vector							
		U_+	U_-	V_+	V_-	W_+	W_-	Z_+	Z_-
U	HS	1	0	0	1	0	1	1	0
U	LS	0	1	1	0	1	0	0	1
V	HS	0	1	1	0	0	1	1	0
V	LS	1	0	0	1	1	0	0	1
W	HS	0	1	0	1	1	0	1	0
W	LS	1	0	1	0	0	1	0	1

HS = High-Side switch, LS = Low-Side switch; 1 = closed, 0 = open

switching action is neglected, the voltage pulses have only discrete amplitudes in time domain. However, the mean value over a PWM period correlates with the desired voltage space vector $\boldsymbol{P}$, which can be assembled by a linear combination of the fundamental voltage space vectors $\boldsymbol{U_+}$, $\boldsymbol{U_-}$, $\boldsymbol{V_+}$, $\boldsymbol{V_-}$, $\boldsymbol{W_+}$, $\boldsymbol{W_-}$ and the zero space vectors $\boldsymbol{Z_+}$, $\boldsymbol{Z_-}$.

$$
\begin{aligned}
\boldsymbol{P} = {} & c_{U_+}\boldsymbol{U_+} + c_{V_+}\boldsymbol{V_+} + c_{W_+}\boldsymbol{W_+} + c_{Z_+}\boldsymbol{Z_+} + \\
& c_{U_-}\boldsymbol{U_-} + c_{V_-}\boldsymbol{V_-} + c_{W_-}\boldsymbol{W_-} + c_{Z_-}\boldsymbol{Z_-}
\end{aligned}
\tag{3}
$$

The coefficients c_{U_+}, c_{U_-}, c_{V_+}, c_{V_-}, c_{W_+}, c_{W_-}, c_{Z_+}, c_{Z_-} define the amplitude of the corresponding fundamental space vectors. In this context, the amplitude of a voltage space vector is equal to the duration of the voltage pulse in the PWM pattern. The choice of the coefficients provides a degree of freedom, which can be used for the fulfillment of the following criteria.

3.1   Design Objectives

1. For achieving a high bandwidth of the current controller, a high maximum modulation amplitude $\|\boldsymbol{P}\|_2$ is desired. Furthermore, it is advantageous if the achievable modulation amplitude is independent of the angle of the voltage space vector, allowing the same dynamic in all space directions.

2. For self-sensing control a minimum pulse width $t_{\mathrm{d}I/\mathrm{d}t}$ is required, to allow a current slope measurement as depicted in Fig. 3. For reasons of symmetry, at least one fundamental voltage space vector of each phase shall obtain the minimum pulse width $t_{\mathrm{d}I/\mathrm{d}t}$.

3. The waveform of the current ripple is affected by the timing sequence of the voltages pulse pattern. Abrupt transitions between modulation patterns can lead to transient deviations in the control current [17]. For enabling a precise current control, the timing sequence must not change for infinitesimal changes of the desired voltage space vector $\boldsymbol{P}$. Therefore, the SVM should be designed in a way that the coefficients of (3) are determined by a continuous function of $\boldsymbol{P}$.

3.2   Design Procedure

The main question of the design of the SVM is the determination of the coefficients from (3), while taking the described design objectives into account. For the following considerations, the convention of Fig. 5 is used for the definition of the angles φ and Φ. The angle φ is defined between the space vector $\boldsymbol{U_+}$ and the desired voltage space vector $\boldsymbol{P}$. Moreover, the sector angle Φ is defined as

$$
\Phi = \frac{\pi}{6}\ \underbrace{\left\lfloor \frac{\varphi}{\frac{\pi}{6}} \right\rfloor}_{\in\{0,1,\ldots,11\}}\ ,\quad 0 \le \varphi < 2\pi
\tag{4}
$$

with the floor function $\lfloor\,\rfloor$. Dividing the set of sector angles into even and odd sectors

$$
\Phi_{even} = \left\{ 2k\,\frac{\pi}{6}\,\middle|\, k = 0..5 \right\}
\tag{5}
$$

$$
\Phi_{odd} = \left\{ (2k+1)\,\frac{\pi}{6}\,\middle|\, k = 0..5 \right\}
\tag{6}
$$
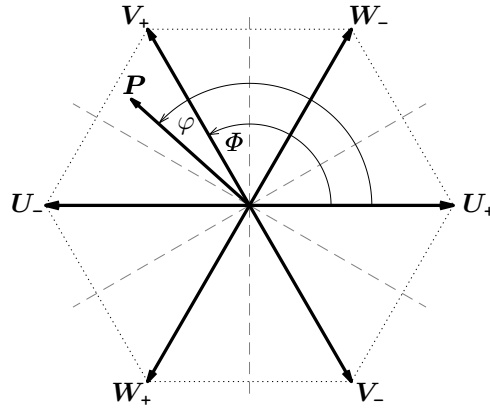
Figure 5: Illustration of the fundamental voltage space vectors and the angles φ, Φ for a desired voltage space vector $\boldsymbol{P}$.

enables the definition of the coordinate transformation

$$\overline{\boldsymbol{P}} = \begin{bmatrix} \cos{(-\vartheta)} & -\sin{(-\vartheta)} \\ \sin{(-\vartheta)} & \cos{(-\vartheta)} \end{bmatrix} \cdot \boldsymbol{P} \tag{7}$$

with

$$\vartheta = \begin{cases} \Phi & \text{for} \quad \Phi \in \Phi_{even} \\ \\ 2\varphi - \Phi - \frac{\pi}{6} & \text{for} \quad \Phi \in \Phi_{odd} \ . \end{cases} \tag{8}$$

Equation (7) transforms the space vector $\boldsymbol{P}$ in a generic coordinate system and has the property that the space vector $\boldsymbol{P}$ can always be transformed to the gray section of Fig. 6. Thus, the
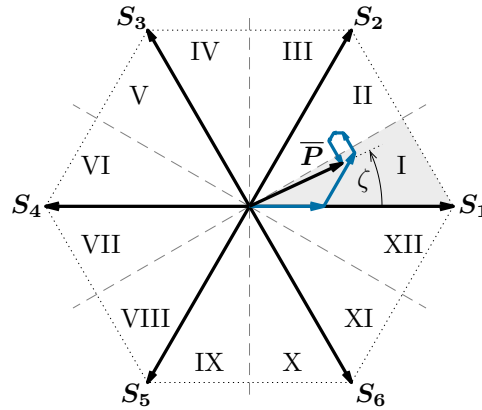

Figure 6: The voltage space vector $\overline{\boldsymbol{P}}$ represents $\boldsymbol{P}$ in a generic coordinate system after the coordinate transformation (7).

resulting space vector $\overline{\boldsymbol{P}}$ can be represented by a linear combination of the generic space vectors $\boldsymbol{S_1}, \ldots, \boldsymbol{S_6}$. The correlation of the generic space vectors to the fundamental space vectors will be discussed later on. The generic coordinate system enables a simplification of the problem (3), because the whole modulation range can be reduced to the gray area of Fig. 6. After solving

the problem in the generic coordinate system, the solution can be transformed back to the respective sector, which is given by Φ. For further considerations, the angle ζ

$$\zeta = \varphi - \vartheta, \quad \zeta \in \left[0, \frac{\pi}{6}\right] \tag{9}$$

is defined as the angle between the space vector $\boldsymbol{S_1}$ and $\overline{\boldsymbol{P}}$ (Fig. 6) and is normalized to an angle of $\pi/6$

$$\hat{\zeta} = \frac{6}{\pi} \zeta \tag{10}$$

for reasons of simplicity. For solving the problem, the coefficients of the space vectors $\boldsymbol{S_1}, \ldots, \boldsymbol{S_6}$ must be determined with regard to the design objectives. In order to achieve a continuous behavior of the voltage pulse pattern, special attention is paid to a sector switchover due to a change of the sector angle Φ. Thus, the following boundaries of the modulation range in Fig. 6 must be considered:

$$B_1 = \left\{\overline{\boldsymbol{P}} \ \middle| \ \left\|\overline{\boldsymbol{P}}\right\|_2 > 0, \ \hat{\zeta} = 1\right\} \tag{11}$$

$$B_2 = \left\{\overline{\boldsymbol{P}} \ \middle| \ \left\|\overline{\boldsymbol{P}}\right\|_2 > 0, \ \hat{\zeta} = 0\right\} \tag{12}$$

$$B_3 = \left\{\overline{\boldsymbol{P}} \ \middle| \ \left\|\overline{\boldsymbol{P}}\right\|_2 = 0, \ \hat{\zeta} \in [0, 1]\right\} \tag{13}$$

The boundary B_1 (B_2) represents a switchover from sector I to sector II (XII), while the boundary B_3 enables a switchover to an arbitrary sector by a transmission via the origin of the coordinate system. Equation (14) shows the designed modulation strategy for the representation of a space vector $\overline{\boldsymbol{P}}$, which is composed as follows:

$$\overline{\boldsymbol{P}} = a_1 \, \boldsymbol{S_1} + a_2 \, \boldsymbol{S_2} + \left(t_{min} + \left(t_{\mathrm{d}I/\mathrm{d}t} - t_{min}\right)\hat{\zeta}\right)\boldsymbol{S_3} + \\ t_{min} \, \boldsymbol{S_4} + t_{min} \, \boldsymbol{S_5} + t_{\mathrm{d}I/\mathrm{d}t} \, \boldsymbol{S_6} \tag{14}$$

In principle, the space vector $\overline{\boldsymbol{P}}$ could be represented just by the space vectors $\boldsymbol{S_1}$ and $\boldsymbol{S_2}$. To enable a current slope measurement in each phase within one PWM period, at least one coefficient of each phase must obtain a minimum amplitude of $t_{\mathrm{d}I/\mathrm{d}t}$. Hence, the space vectors $\boldsymbol{S_1}$, $\boldsymbol{S_2}$ and $\boldsymbol{S_6}$ are chosen for the current slope measurement, because the linear combination of the vectors already shows in a similar direction to $\overline{\boldsymbol{P}}$, meeting the demand of a high modulation amplitude. Consequently, the space vectors $\boldsymbol{S_1}$, $\boldsymbol{S_2}$ and $\boldsymbol{S_6}$ are desired with an amplitude of at least $t_{\mathrm{d}I/\mathrm{d}t}$.

In the first step, the coefficient of $\boldsymbol{S_6}$ is set to $t_{\mathrm{d}I/\mathrm{d}t}$ and it is assumed that the coefficients a_1 and a_2 obtain an amplitude greater than $t_{\mathrm{d}I/\mathrm{d}t}$. The validity of this assumption will be proven later on. The coefficients of non-required space vectors ($\boldsymbol{S_4}$, $\boldsymbol{S_5}$) are set to t_{min} to ensure a minimum pulse width. The minimum pulse width t_{min} avoids very short voltage pulses, which may cause problems for semiconductor switches. Concerning a transition between sectors, the space vector $\boldsymbol{S_3}$ plays an important role for a jerk-free sector switchover. An evaluation of (14) at the boundary B_1 indicates

$$\overline{\boldsymbol{P}}_{B_1} = a_1 \, \boldsymbol{S_1} + a_2 \, \boldsymbol{S_2} + t_{min}\left(\boldsymbol{S_4} + \boldsymbol{S_5}\right) + t_{\mathrm{d}I/\mathrm{d}t}\left(\boldsymbol{S_3} + \boldsymbol{S_6}\right) \tag{15}$$

that pairs of space vectors $\{\boldsymbol{S_1}, \boldsymbol{S_2}\}$, $\{\boldsymbol{S_4}, \boldsymbol{S_5}\}$, $\{\boldsymbol{S_3}, \boldsymbol{S_6}\}$ have the same coefficients ($a_1 = a_2$ by constraint of boundary). Due to the symmetric arrangement of the coefficients, a continuous

switchover from sector I to sector II is possible by swapping the generic space vectors of the pairs $(S_1 \to S_2, S_2 \to S_1, \dots)$. Concerning the boundary B_2,

$$\overline{P}_{B_2} = a_1\, S_1 + a_2\, S_2 + t_{min}\,(S_3 + S_4 + S_5) + t_{\mathrm{d}I/\mathrm{dt}}\, S_6 \tag{16}$$

the pairs of space vectors $\{S_2, S_6\}$ and $\{S_3, S_5\}$ have the same coefficients ($a_2 = t_{\mathrm{d}I/\mathrm{dt}}$ by constraint of boundary). Therefore, also in this case, a continuous switchover from sector I to sector XII is possible by swapping the generic space vectors of the outlined space vector pairs. The relevance of the boundary B_3 will be shown after solving (14). The coefficients a_1 and a_2 can be directly calculated by converting (14) to the following form:

$$\begin{bmatrix} a_1 \\ a_2 \end{bmatrix} = \begin{bmatrix} S_1 & S_2 \end{bmatrix}^{-1} \cdot \left(\overline{P} - \left(t_{min} + \left(t_{\mathrm{d}I/\mathrm{dt}} - t_{min} \right) \hat{\zeta} \right) S_3 - t_{min}\, S_4 - t_{min}\, S_5 - t_{\mathrm{d}I/\mathrm{dt}}\, S_6 \right) \tag{17}$$

Thus, the space vector $\overline{P}$ can be represented by (18)

$$\overline{P} = \bar{c}_1\, S_1 + \bar{c}_2\, S_2 + \bar{c}_3\, S_3 + \bar{c}_4\, S_4 + \bar{c}_5\, S_5 + \bar{c}_6\, S_6 \tag{18}$$

with the coefficient vector

$$\bar{c} = \begin{bmatrix} \bar{c}_1 & \bar{c}_2 & \bar{c}_3 & \bar{c}_4 & \bar{c}_5 & \bar{c}_6 \end{bmatrix}^T . \tag{19}$$

The coefficients of (19) must fulfill the constraint that the sum

$$\sum_{i=1}^{6} \bar{c}_i = 1 \tag{20}$$

is equal to 1. This constraint procures that the whole PWM period is filled by the voltage space vectors, which is a consequence of a constant PWM switching frequency. For that reason, the remaining time

$$t_{rem} = 1 - \left(a_1 + a_2 + t_{\mathrm{d}I/\mathrm{dt}} + 3\, t_{min} + \left(t_{\mathrm{d}I/\mathrm{dt}} - t_{min} \right) \hat{\zeta} \right) \tag{21}$$

is distributed equally among all generic voltage space vectors, to allow a maximum measurement window for $\mathrm{d}\Delta I/\mathrm{dt}$ measurements. Thus, the coefficients of $\bar{c}$ are given by a coefficient comparison between (14) and (18),

$$\bar{c} = \begin{bmatrix} a_1 \\ a_2 \\ t_{min} + \left(t_{\mathrm{d}I/\mathrm{dt}} - t_{min} \right) \hat{\zeta} \\ t_{min} \\ t_{min} \\ t_{\mathrm{d}I/\mathrm{dt}} \end{bmatrix} + \frac{t_{rem}}{6} \begin{bmatrix} 1 \\ 1 \\ 1 \\ 1 \\ 1 \\ 1 \end{bmatrix} \tag{22}$$

with an extension by the value of $t_{rem}/6$. The additional amplitude of $t_{rem}/6$ does not influence the representation of $\overline{P}$ because it is equally distributed to all space directions, which results in a composed zero space vector. Figure 7 shows the admissible modulation area, which is located inside the red boundaries. The minimum and maximum symmetrical modulation amplitude (R_{min}, R_{max}) define the symmetrical modulation area, which is indicated by the gray area. The limitation of the admissible modulation area to the symmetrical modulation area provokes that the current controller obtains the same dynamic in all space directions. It can be seen that the symmetrical modulation area does not include the origin of the modulation area for the chosen parameters $t_{\mathrm{d}I/\mathrm{dt}} = 0.14$ and $t_{min} = 0.02$ (parameters are normalized to PWM period).
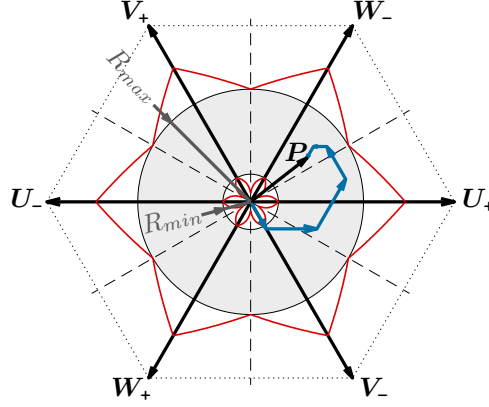
Figure 7: SVM by Equ. (14): Illustration of the possible symmetrical modulation range (gray area) with the minimum and maximum modulation boundaries (red). ($t_{\mathrm{d}I/\mathrm{d}t} = 0.14$, $t_{min} = 0.02$)
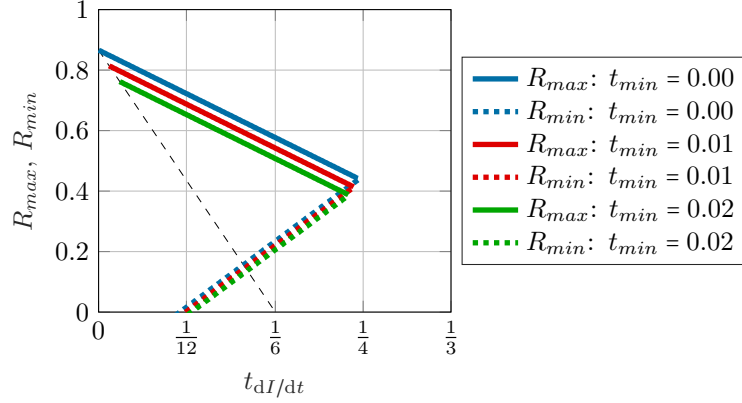

Figure 8: Comparison of the symmetrical modulation amplitude for the designed space vector modulation.

Figure 8 shows the symmetrical modulation amplitudes as a function of $t_{\mathrm{d}I/\mathrm{d}t}$ for fixed values of t_{min}. It can be seen that the maximum symmetrical modulation amplitude R_{max} decreases with a higher value of $t_{\mathrm{d}I/\mathrm{d}t}$. At a certain value of $t_{\mathrm{d}I/\mathrm{d}t}$, also a minimum symmetrical modulation amplitude R_{min} occurs, which is an issue for small amplitudes of $\overline{\boldsymbol{P}}$.

For that reason, the calculation approach of (14) is extended for dealing with small modulation amplitudes. Equation (23) shows an alternative set of coefficients for the representation of $\overline{\boldsymbol{P}}$

$$\hat{\boldsymbol{c}} = \frac{1}{6} \cdot \boldsymbol{T}^{6 \times 1} + \frac{1}{3} \left[\boldsymbol{S_1} \ \boldsymbol{S_2} \ \boldsymbol{S_3} \ \boldsymbol{S_4} \ \boldsymbol{S_5} \ \boldsymbol{S_6} \right]^T \cdot \overline{\boldsymbol{P}} \tag{23}$$

with a 6×1 matrix $\boldsymbol{T}^{6 \times 1}$ with all entries chosen as 1. The calculation (23) has the property that each coefficient has an offset of 1/6, which is superposed by the inner product $\overline{\boldsymbol{P}}$ and the corresponding space vector $\boldsymbol{S}$. Thus, all coefficients have the amplitude of 1/6 if the amplitude of $\overline{\boldsymbol{P}}$ is zero ($\left\| \overline{\boldsymbol{P}} \right\|_2 = 0$). This characteristic is appropriate for a continuous sector switchover at the boundary B_3 (13), because with an equal amplitude the mapping between the coefficients (23) and the fundamental space vectors can be done in any order (Equ. (23) also fulfills the

boundaries B_1 and B_2). For the design of a SVM without restrictions for small modulation amplitudes as shown in Fig. 8, the coefficients of (19) and (23) are combined

$$\boldsymbol{c} = \alpha\,\bar{\boldsymbol{c}} + (1 - \alpha)\,\hat{\boldsymbol{c}} \tag{24}$$

by a weighting factor α. The weighting factor α

$$\alpha = \frac{\|\boldsymbol{P}\|_2}{R_{max}} \tag{25}$$

is amplitude dependent by $\|\boldsymbol{P}\|_2$ and normalized to R_{max}. Therefore, the SVM of (23) is dominant for low amplitudes and the modulation strategy (19) is dominant for large amplitudes of $\|\boldsymbol{P}\|_2$. Regarding the transition between two modulation strategies, it must be checked that all coefficients obtain at least an amplitude of t_{min} within the modulation range. Furthermore, at least one coefficient of each phase direction must allow a $\mathrm{d}\Delta I/\mathrm{d}t$ measurement by an amplitude of at least $t_{\mathrm{d}I/\mathrm{d}t}$. This circumstance was proven with a numerical simulation over the whole admissible modulation area. With the coefficients of (24), the desired voltage space vector $\overline{\boldsymbol{P}}$ can be composed as

$$\overline{\boldsymbol{P}} = c_1\,\boldsymbol{S_1} + c_2\,\boldsymbol{S_2} + c_3\,\boldsymbol{S_3} + c_4\,\boldsymbol{S_4} + c_5\,\boldsymbol{S_5} + c_6\,\boldsymbol{S_6}. \tag{26}$$

This kind of SVM will be stated as 6-Active HMR SVM (High Modulation Range) in the following considerations. The term "6-Active" refers to the number of active space vectors within a PWM period. Figure 9 shows the possible modulation range for the 6-Active HMR
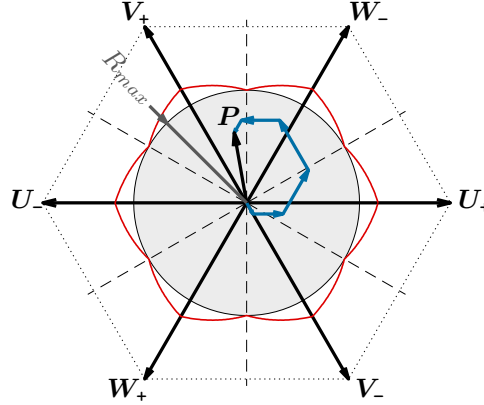

Figure 9: 6-Active HMR SVM: Illustration of the possible symmetrical modulation range (gray area) with the corresponding maximum modulation boundary (red). The origin of the coordinate system is included in the admissible modulation range. ($t_{\mathrm{d}I/\mathrm{d}t} = 0.14$, $t_{min} = 0.02$)

SVM. In contrast to Fig. 7, the admissible modulation range also includes the origin of the coordinate system. Considering the possible modulation range, Fig. 10 depicts the maximum symmetrical modulation range as a function of $t_{\mathrm{d}I/\mathrm{d}t}$ for the modulation strategy (26).
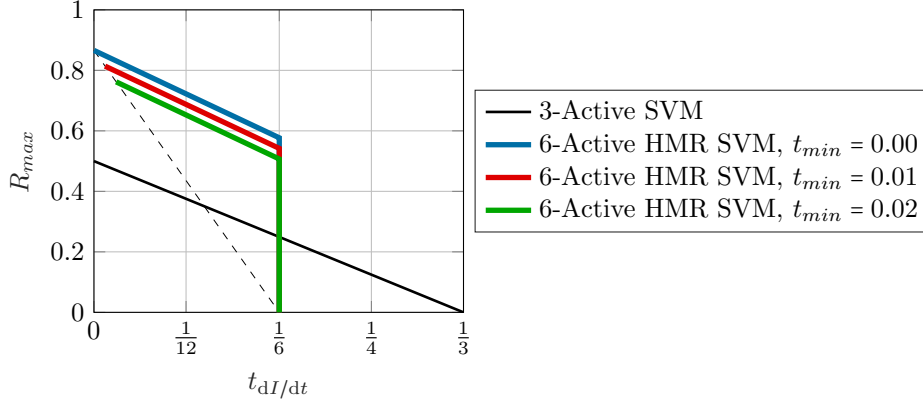
Figure 10: Comparison of the symmetrical modulation amplitude for the 6-Active HMR SVM.

In contrast to Fig. 8, the 6-Active HMR SVM has the advantage of $R_{min} = 0$ in the admissible range of $t_{dI/dt}$. For reasons of comparison, the characteristic of the 3-Active SVM is also shown, which was used in previous studies for self-sensing control [16]. Concerning the modulation amplitude, the 6-Active HMR SVM enables a significant higher value of R_{max} compared to the 3-Active SVM, which allows a higher dynamic in current control.

Equation (26) shows the coefficients of the SVM in the generic coordinate system, which was introduced with the coordinate transformation (7). However, the coefficients of the fundamental space vectors $\boldsymbol{U_+}$, $\boldsymbol{U_-}$, $\boldsymbol{V_+}$, $\boldsymbol{V_-}$, $\boldsymbol{W_+}$, $\boldsymbol{W_-}$ have to be determined for an implementation of the SVM in a DSP. The coefficients of (3) are determined by a back transformation of the generic space vector coefficients. Therefore, the coefficients of the fundamental space vectors c_{U_+}, c_{U_-}, c_{V_+},

Table 2: Coefficient Mapping

Coeff.	Sector angle Φ											
	$0\frac{\pi}{6}$	$1\frac{\pi}{6}$	$2\frac{\pi}{6}$	$3\frac{\pi}{6}$	$4\frac{\pi}{6}$	$5\frac{\pi}{6}$	$6\frac{\pi}{6}$	$7\frac{\pi}{6}$	$8\frac{\pi}{6}$	$9\frac{\pi}{6}$	$10\frac{\pi}{6}$	$11\frac{\pi}{6}$
c_{U_+}	c_1	c_2	c_6	c_3	c_5	c_4	c_4	c_5	c_3	c_6	c_2	c_1
c_{W_-}	c_2	c_1	c_1	c_2	c_6	c_3	c_5	c_4	c_4	c_5	c_3	c_6
c_{V_+}	c_3	c_6	c_2	c_1	c_1	c_2	c_6	c_3	c_5	c_4	c_4	c_5
c_{U_-}	c_4	c_5	c_3	c_6	c_2	c_1	c_1	c_2	c_6	c_3	c_5	c_4
c_{W_+}	c_5	c_4	c_4	c_5	c_3	c_6	c_2	c_1	c_1	c_2	c_6	c_3
c_{V_-}	c_6	c_3	c_5	c_4	c_4	c_5	c_3	c_6	c_2	c_1	c_1	c_2
c_{Z_+}	0	0	0	0	0	0	0	0	0	0	0	0
c_{Z_-}	0	0	0	0	0	0	0	0	0	0	0	0

c_{V_-}, c_{W_+}, c_{W_-}, c_{Z_+}, c_{Z_-} are determined by a sector angle dependent mapping of the coefficients of (26) by means of Table 2. Regarding self-sensing, at least three current slope measurements are desired within one PWM period. Figure 11 shows the number of achievable current slope measurements within one PWM period for different modulation regions. It can be seen that the inner regions of the modulation area allow more than three current slope measurements. The additional information could be used for increasing the quality of the self-sensing position signal.
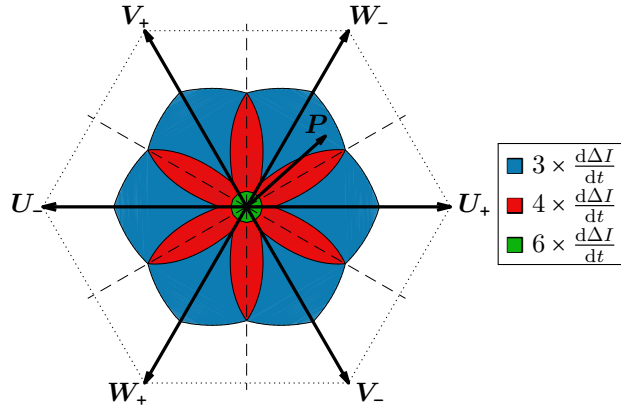
Figure 11: 6-Active HMR SVM: Visualization of the number of possible $\mathrm{d}\Delta I/\mathrm{d}t$ measurements for different modulation regions. ($t_{\mathrm{d}I/\mathrm{d}t} = 0.14$, $t_{min} = 0.02$)

4 Measurements and Results

The following section contains measurement results of the introduced space vector modulation strategy. Therefore, the SVM was implemented on a three-phase inverter with a TMS320F28335 digital signal processor from Texas Instruments. The current controller is based on the control structure as shown in Fig. 4. In this configuration, only the DC-Link current was measured and the phase currents (I_U, I_V, I_W) were calculated and transformed in a Cartesian coordinate system (I_x, I_y) by the Clarke transformation. The control law of the control currents I_x, I_y was based on non-coupled proportional integral (PI) controllers. In the following, all measurements were performed on a radial homopolar AMB as shown in Fig. 1. The six-pole AMB was driven by a three-phase inverter with a DC-Link voltage of $U_{DC} = 18\,V$. The parameters of the SVM were chosen as $f_{PWM} = 20\,kHz$, $t_{\mathrm{d}I/\mathrm{d}t} = 0.14$ and $t_{min} = 0.02$. This configuration avoids voltage pulses shorter than $1\,\mu s$ and provides at least $7\,\mu s$ duration for current slope measurements.
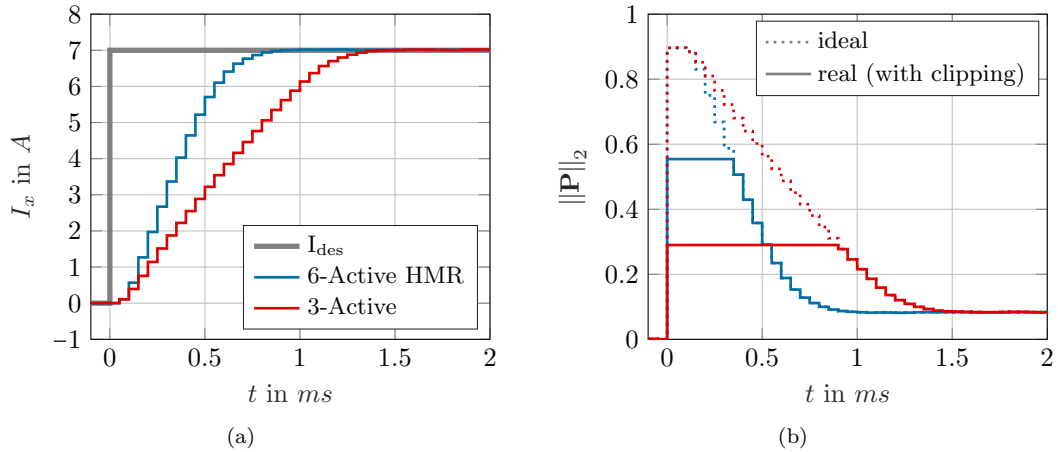

(a)

(b)

Figure 12: (**a**) Measured step response of the current controller for different modulation strategies. (**b**) Corresponding amplitude of the desired voltage space vector $\boldsymbol{P}$.
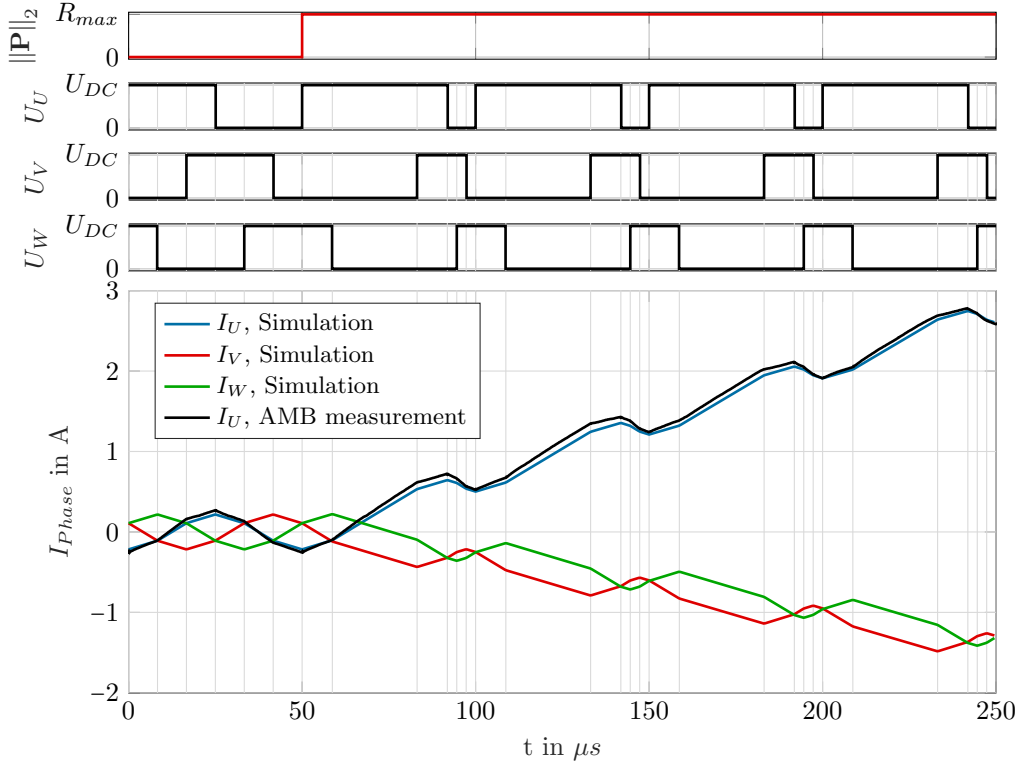
Figure 13: Modulation pattern of the 6-Active HMR SVM: Illustration of the phase voltages and currents for a step in the amplitude of $\boldsymbol{P}$ from zero to R_{max} ($\varphi = 0$).

Figure 13 shows the operation of the designed SVM in time domain with the respective phase voltages and currents. The desired voltage space vector $\boldsymbol{P}$ was chosen as a step from zero to the maximal symmetrical amplitude R_{max} in direction of $\boldsymbol{U}+$ ($\varphi = 0$). The phase voltages U_U, U_V and U_W depict the timing of the voltage pulse pattern corresponding to $\boldsymbol{P}$. It can be seen that always six space vectors are active within one PWM period. In case of $\|\boldsymbol{P}\|_2 = 0$, all space vectors obtain the same amplitude, which results in zero mean value of the phase voltages in contrast to the case of $\|\boldsymbol{P}\|_2 = R_{max}$. The bottom plot shows a comparison between a simulation and a measurement on the AMB prototype for the phase U. Although measurement and simulation show good consistency, a remaining deviation can be seen because of parameter uncertainties and non-linear AMB material effects. Regarding self-sensing operation, the SVM enables at least one $\mathrm{d}\Delta I/\mathrm{d}t$ measurement per phase in each PWM period (Fig. 3), which can be used for self-sensing position detection.

An adequate bandwidth of the current controller is important to follow the requirements of superimposed force and position controllers. Figure 12 shows a measurement of the current controller step response for different SVMs. The 3-Active SVM has already been investigated in previous work [16] and is therefore used as reference. It can be seen that the 6-Active HMR SVM achieves a fast current response without overshoot. A comparison of the maximum space vector amplitude $\|\overline{\boldsymbol{P}}\|_2$ indicates that the 6-Active HMR modulation has about 90% more modulation amplitude than the 3-Active SVM for the chosen parameters $t_{\mathrm{d}I/\mathrm{d}t}$ and t_{min}. A bigger modulation amplitude can be used to increase the dynamic of the current controller or

to reduce the DC-link voltage in order to minimize power losses in the AMB without losing control bandwidth.
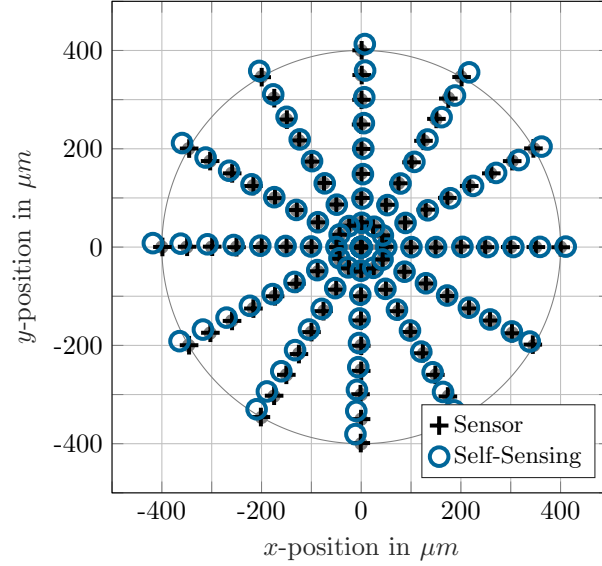

Figure 14: Comparison of the self-sensing and sensor position for different rotor setpoints.

Concerning self-sensing position control, the AMB was operated with a position estimator, which uses the $\mathrm{d}\Delta I/\mathrm{d}t$ information obtained by the 6-Active HMR SVM. Figure 14 shows a comparison of the self-sensing and sensor position of a levitating rotor, whereby the AMB prototype has an air gap of $800\,\mu m$. The steady-state error between the sensor and self-sensing method shows an overall low error with slight amplitude and angle deviations in the outer regions.

5   Conclusions

The focus of this study lied on the design of a space vector modulation for a three-phase self-sensing radial magnetic bearing. In contrast to conventional SVM methods, the design of the SVM in this study underlies additional restrictions to allow a self-sensing operation of the magnetic bearing. Special attention was paid to the modulation amplitude for achieving a high dynamic of a superimposed current controller. Furthermore, considerations concerning precise current control were taken into account. This work contains the principles of self-sensing space vector modulation with a detailed description of a novel self-sensing SVM strategy. The designed SVM strategy was implemented and verified on a three-phase inverter in combination with a prototype of a self-sensing magnetic bearing. Measurements on the prototype showed that the dynamic of the current controller could be increased compared to a previous modulation strategy. Finally, a measurement with different setpoints of a levitating rotor showed the steady-state performance of the self-sensing control compared to an external sensor. Further analysis on the quality of the self-sensing position detection, especially under dynamic conditions, will be part of future investigations.

References

[1] H. Bleuler, D. Vischer, G. Schweitzer, A. Traxler, and D. Zlatnik. New concepts for cost-effective magnetic bearing control. Automatica, Vol. 30, No. 5, pp. 871–876, May 1994.

[2] E. H. Maslen. Self–sensing for active magnetic bearings: overview and status. Proc. 10th International Symposium on Magnetic Bearings (ISMB10), Martigny, Switzerland, 21–23 Aug. 2006.

[3] T. Glück, W. Kemmetmüller, C. Tump, and A. Kugi. A novel robust position estimator for self-sensing magnetic levitation systems based on least squares identification. Control Engineering Practice, Vol. 19, No. 2, pp. 146–157, Feb. 2011.

[4] T. Mizuno, T. Ishiim, and K. Araki. Self-sensing magnetic suspension using hysteresis amplifiers. Control Engineering Practice, Vol. 6 No. 9, pp. 1133–1140, Sept. 1998.

[5] T. Mizuno and Y. Hirasawa. Self-sensing magnetic suspension using an H-bridge type hysteresis amplifier operating in two quadrants. Proc. 28th IEEE IECON, pp. 1818–1823, Nov. 2002.

[6] J.-S. Yim, J.-H. Kim, S.-K. Sul, H.-J. Ahn, and D.-C. Han. Sensorless Position Control of Active Magnetic Bearings Based on High Frequency Signal Injection method. Proc. 18th Annu. IEEE APEC, Vol. 1, pp. 83–88, Feb. 2003.

[7] P. Garcia, J. M. Guerrero, F. Briz, and D. D. Reigosa. Sensorless Control of Three-Pole Active Magnetic Bearings Using Saliency-tracking Based Methods. IEEE Transactions on Industry Applications, Vol. 46, No. 4, pp. 1476–1484, Jul.-Aug. 2010.

[8] W. Gruber, M. Pichler, M. Rothböck, and W. Amrhein. Self-Sensing Active Magnetic Bearing Using 2-Level PWM Current Ripple Demodulation. Proc. 7th International Conference on Sensing Technology (ICST), Wellington, New Zealand, Dec. 2013.

[9] J. Wang and A. Binder. Position estimation for self-sensing magnetic bearings based on the current slope due to the switching amplifier. Eur. Power Electr. and Drives (EPE), Vol 26., No. 4, pp. 15–141, 2016.

[10] A.C, Niemann, G. Van Schoor, and C.P. Du Rand. Self-Sensing Active Magnetic Bearing Based on a Direct Current Measurement Approach. MDPI, Sensors, Vol. 13, No. 9, 2013.

[11] Y. Jiang, K. Wang, M. Sun, and J. Xie. Displacement Self-Sensing Method for AMB-Rotor Systems Using Current Ripple Demodulations Combined With PWM Command Signals. IEEE Sensors Journal, Vol. 19, No. 14, Jul. 2019.

[12] E. O. Ranfta, G. van Schoor, and C. P. du Rand. An Integrated Self-Sensing Approach for Active Magnetic Bearings. SAIEE Africa Research Journal, Vol. 102, No. 4, Dec. 2011.

[13] Y. Jiang, X. Ma, and Y. Fan. Rotor Displacement Self-Sensing Approach for Permanent Magnet Biased Magnetic Bearings Using Double-Axis PWM Demodulation. IEEE Sensors Journal, Vol. 18, No. 19, Oct. 2018.

[14] M. Schrödl. Sensorless control of AC machines at low speed and standstill based on the "INFORM" method. IAS '96. Conference Record of the 1996 IEEE Industry Applications Conference Thirty-First IAS Annual Meeting, San Diego, CA, USA, 6-10 Oct. 1996.

[15] M. Hofer, M. Hutterer, T. Nenning, and M. Schrödl. Improved Sensorless Control of a Modular Three Phase Radial Active Magnetic Bearing. Proc. 14th International Symposium on Magnetic Bearings (ISMB14), Linz, Austria, 11–14 Aug. 2014.

[16] T. Nenning, M. Hofer, M. Hutterer, and M. Schrödl. Setup with two Self-Sensing Magnetic Bearings using Differential 3-Active INFORM. Proc. of the 14th International Symposium on Magnetic Bearings (ISMB14), Linz, Austria, 11–14 Aug. 2014.

[17] D. Wimmer, M. Hutterer, M. Hofer, and M. Schrödl. Space Vector Modulation Strategies for Self-Sensing Three-Phase Radial Active Magnetic Bearings. MDPI Actuators, Vol. 8, No. 2, 2019.

[18] D. Wimmer, M. Hutterer, and M. Schrödl. Design and Analysis of a PCB Integrated Differential Current Slope Sensor with Ferrite Support for High dV/dt Operations. PCIM Europe digital days 2021, Nuremberg, Germany, 3–7 May 2021.